

# STATISTICAL STRENGTH OF HIERARCHICAL CARBON NANOTUBE COMPOSITES

X. Frank Xu,<sup>1,\*</sup> Keqiang Hu,<sup>1</sup> Irene J. Beyerlein,<sup>2</sup> & George Deodatis<sup>3</sup>

<sup>1</sup>Department of Civil, Environmental & Ocean Engineering, Stevens Institute of Technology, Hoboken, New Jersey, 07307, USA

<sup>2</sup>Theoretical Division, Los Alamos National Laboratory, Los Alamos, New Mexico, 87545, USA

<sup>3</sup>Department of Civil Engineering and Engineering Mechanics, Columbia University, New York, New York, 10027, USA

Original Manuscript Submitted: 8/24/10; Final Draft Received: 12/12/10

*In modeling and simulation of material failure, a major challenge lies in the computation of stress redistributions during the stochastic propagation of localized failures. In this study, an  $n^{\text{th}}$ -order generalized local load sharing (GLLS) model is introduced to account for the complexity of such local interactions in an efficient way. The rule is flexible, covering a wide range of load sharing mechanisms between the equal load sharing and local load sharing types. A Monte Carlo simulation model employing various orders of this GLLS rule is used to study the effect of such load redistributions on the failure of a micron-scale carbon nanotube (CNT) fiber. These CNT fibers exhibit a hierarchical structure. At the lowest length scale are single- or multi-walled CNTs with nanoscale diameters (e.g., 1–10 nm), which are aligned and clustered to form small bundles at the next higher length scale (15–60 nm in diameter). Thousands of these CNT bundles aggregate and align to create CNT fibers with micron-scale diameters. The results of this study indicate that the mean strength of the CNT fibers reduces by approximately two-thirds of an order of magnitude when up-scaling from an individual CNT to a CNT fiber. This dramatic strength reduction occurs at three different stages of the up-scaling process: (1) from individual CNTs of length  $l_t$  to CNT bundles of the same length; (2) from a CNT bundle of length  $l_t$  to a CNT bundle of length  $l_b$  ( $l_b=10l_t$ ); and (3) from CNT bundles of length  $l_b$  to CNT fibers of the same length. The specific strength reductions during these three stages are provided in the paper. The computed fiber strengths are in the same general range as corresponding experimental values reported in the literature. The ability of the GLLS model to efficiently account for different mechanisms of load sharing, in combination with the multi-stage up-scaling Monte Carlo simulation approach, is expected to benefit the design and optimization of robust structural composites built up from carbon nanotubes.*

**KEY WORDS:** load sharing models, statistical size effect, statistical failure, carbon nanotubes, hierarchical structure, Monte Carlo simulation

## 1. INTRODUCTION

In a typical failure scenario of solids under stress, accumulation of atomic scale instabilities triggers nucleation of micro-flaws and micro-voids; the growth and coalesce of the latter leads to formation of macroscopic cracks and ultimately results in a catastrophic rupture. Such a complex failure process involves (1) a large number of fine-scale field quantities representing both material and mechanical forcing components, and (2) the quasi-static or dynamical evolution of these quantities at multiple length scales. Direct quantification or measurement of these field quantities in space and time is challenging, if not impossible in some cases. In this sense, probabilistic descriptions and uncertainty

---

\*Correspond to X. Frank Xu, E-mail: x.xu@stevens.edu, URL: <http://personal.stevens.edu/~xxu1>

quantification models are of paramount importance in the design of robust advanced materials and reliable prediction of the stresses and strains at failure.

Recent dramatic progress in multi-scale research is closely connected with the rapid growth of nanotechnology starting in the 1990s. Most bottom-up multi-scale modeling strategies involve passing information regarding defects, microstructure, and their interactions from the atomic scale to the micro-scale and eventually to the macro-scale. To date, determinism has remained an almost universal strategy in most of these models, in which average properties, constants, or representative unit processes are transferred up through the scales. While this approach works well when the material response of interest is stable, such as in linear elasticity or small-scale plasticity, it becomes a severe limitation when material behavior is governed by the onset of inhomogeneities and instabilities. Defects and microstructure at all length scales are random in nature and failure properties, such as peak stress or peak strain, are highly sensitive to these uncertainties. A deterministic simulation merely corresponds to a single point in the random space of failure stress or strain and does not offer reliability or sensitivity information. To understand and quantify uncertainty at different length scales and study how it impacts phenomena operating at other length scales, one needs to develop a multi-scale stochastic modeling strategy to account for incomplete microstructure information, statistical defects, random failure initiation, stochastic progression, large sample sets or ensemble, and scaling laws [1–6].

In modeling and simulation of material failure, a major challenge lies in the computation of stress redistribution or in establishing a local load sharing rule during the nucleation and propagation of localized failure events. Considering the large defect and micro-structural parameter space, as well as the need to simulate a very large number of samples for each parameter set, it becomes prohibitively expensive computationally to employ sophisticated mechanics models. Consequently, it becomes highly desirable to seek empirical, but accurate and efficient, surrogate load sharing models as an alternative. The main objective of this paper is to introduce such a surrogate model—namely, an  $n^{\text{th}}$ -order one-dimensional (1D) and two-dimensional (2D) generalized local load sharing (GLLS) model—and to apply it in simulation to study the statistical strength of micron-scale carbon nanotube (CNT) fibers. The characteristics of load redistribution can be altered by the order  $n$  of the GLLS rule, which can vary from ductile-like (diffuse) to brittle-like (localized). The CNT fibers have a complex hierarchical nanostructure consisting of thousands of CNT bundles, which in turn consist of dozens of CNTs. Each CNT has random strength that leads to random strength bundles, which in turn leads to random strength CNT fibers. As the size scale increases, the mean strength and variance are predicted in this study to decrease in a manner that depends on the details of the load redistribution (order  $n$ ). At the end, model predictions are compared with some data found in the literature and recommendations for future extensions are provided.

## 2. GENERALIZED LOCAL LOAD SHARING MODEL

Originally introduced to explain ruptures of bundles of threads [7], fiber bundle models have been applied to problems involving cracks and fractures, earthquakes, and other breakdown phenomena. In such models, the fibers are usually assumed to be aligned and loaded with the same force along the fiber direction. The strengths of the fibers are modeled as independent and identically distributed random variables. Consequently, as the applied load increases, the weakest fiber will break first. The load carried by this weakest fiber prior to failure is redistributed among the surviving ones. The nature of this redistribution reflects the interaction of the components in a system.

To circumvent complex and time-consuming mechanics-based calculations for load redistribution following fiber breaks, load sharing rules are employed. The two classical load sharing rules are the equal load sharing (ELS) rule [7], where the load is uniformly (equally) distributed among all intact fibers, and the extreme local load sharing (ELLS) rule [8, 9], where the broken fiber affects only the nearest surviving fibers. Although the mechanics are only approximated, these rules can make possible relating analytically stochastic failure processes to statistical strength. For instance, to relate load sharing to probabilistic bundle strength, Harlow and Phoenix [8, 9] proposed a simple ELLS rule for 1D systems by transferring the load only to the two nearest surviving bonds. As a result, exact recursion relations were established. Their work was later extended to account for the next-nearest neighbors by Phoenix and Beyerlein [10].

In actuality, load redistribution lies in between the limits of ELS and ELLS. The variation is very broad and the extent of re-distribution depends on many material/system parameters. Hedgepeth and Van Dyke [11] developed a

shear lag model to compute the stress concentration factors as a result of a 1D row of breaks (cracks) by assuming the elastically deforming matrix only serves as shear coupling between neighboring fibers. The Hedgepeth and Van Dyke model was later extended to treat a general arrangement of fiber breaks [12] showing that details of stress fields caused by breaks depend on the properties of the fiber, matrix, and fiber-matrix interface deformation.

In order to provide an efficient load sharing rule that can span the range between ELS and ELLS, an  $n^{th}$ -order GLLS model is proposed in this study (a thermodynamic formulation will be reported in a separate paper). The two limiting cases of the GLLS model, the zeroth-order GLLS and sufficiently high-order GLLS, reduce to the ELS model [7] and ELLS model [8, 9], respectively. Instead of directly simulating a failure process for different material microstructure parameters, the GLLS model introduces simple rules that can be empirically calibrated to account for a variety of complex local interactions. In this way, GLLS helps to circumvent the issue of *incomputability* [13] in nonlinear mechanics or the so-called “curse-of-dimensionality” in mathematics.

## 2.1 An Illustrative Elastic Beam Model

To illustrate the mechanisms behind the rules used in GLLS, a problem involving load redistribution in an elastic beam-spring assembly is considered first. The elastic beam model consists of a large number of parallel and aligned elastic springs attached to two parallel beams. The lower and upper beams are modeled as perfectly rigid and elastic, respectively. The springs, with identical length at rest, behave linearly elastic until breaking at a certain strength limit under an incremental load. When a spring is broken, the released force serves as an upward perturbing force acting on the upper beam. The resulting deformation of the upper beam leads to redistribution of this force among the remaining intact springs, which determines the local load sharing rule.

For an infinitely long elastic beam lying on elastic springs with spacing  $l$ , following classical beam theory, the Green’s function is analytically given as

$$G(x) = \frac{\lambda l}{2k} e^{-\lambda|x|} [\cos(\lambda x) + \sin(\lambda |x|)] \quad (1)$$

which corresponds to the deformation of the beam at location  $x$  due to a unit point force applied at the origin. Parameter  $\lambda = (k/4lEI)^{1/4}$  indicates the degree of localization, with  $EI$  and  $k$  denoting the bending stiffness of the beam and the elastic constant of the springs, respectively. For sufficiently small  $\lambda$ , the deflection becomes almost identical throughout the beam, and the redistribution of the force corresponds to the ELS rule. As parameter  $\lambda$  increases, the size of the neighborhood participating in load sharing is reduced, and the load sharing becomes more localized, approaching the ELLS model. This trend is illustrated in Fig. 1 where beam deflection profiles resulting from a broken spring at  $x = 0$  are graphed for different values of  $\lambda$ . Consequently, with the use of a single parameter  $\lambda$ , a wide range of load redistribution patterns can be obtained between the two extreme cases of ELLS and ELS.

## 2.2 Generalized Local Load Sharing Rules

This section describes the  $n^{th}$ -order GLLS model for 1D and 2D systems. The familiar ELLS model is described first in order to distinguish it from the  $n^{th}$ -order nearest neighbor GLLS.

### 2.2.1 One-Dimensional ELLS Model

Consider a 1D system of bonds in which load sharing follows the ELLS rule [8, 9]. As shown in Fig. 2(a), when the central bond is broken, the load released from the broken bond is shared equally by the two nearest-neighboring bonds. If any of the nearest-neighboring bonds are already broken [Fig. 2(b)], the load meant to be redistributed to this bond will be equally shared by its two nearest neighbors. This load sharing process continues iteratively. The criterion for the iterations to stop is when the shared load on any broken bond becomes negligibly small. Analytical expressions can be established for the load distribution ratios of the 1D ELLS model. For example, for the case shown in Fig. 2(b), the ratios of the load distributed to the nearest surviving bonds to the left and to the right are calculated as

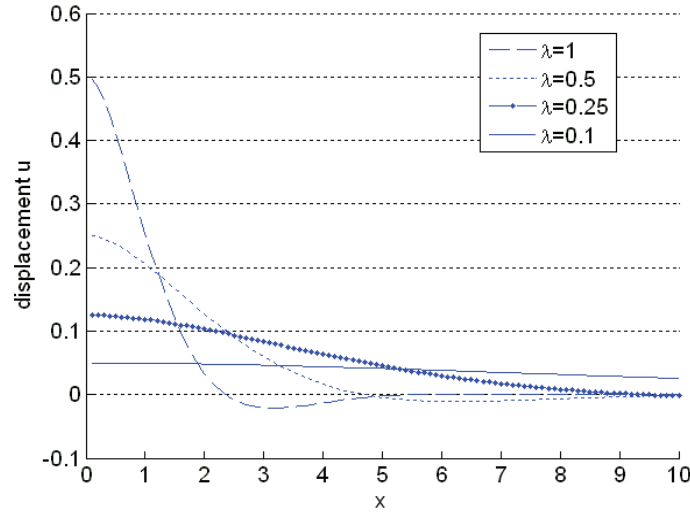


**FIG. 1:** Beam deflection profiles resulting from a broken spring at  $x = 0$  for different values of the localization parameter  $\lambda$  ( $k = 1, l = 1$ ).

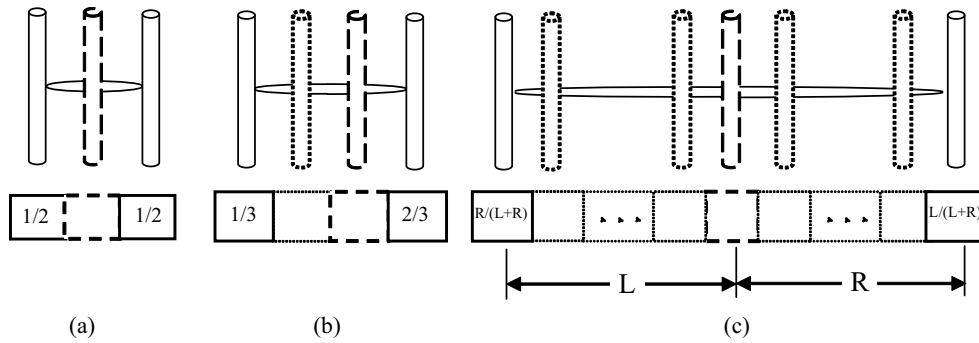


**FIG. 2:** Schematic of the load distribution for the 1D ELLS model (continuous, intact bonds; dashes, current broken bonds; dots, pre-existing broken bonds).

$$r_L = \sum_{i=1}^{\infty} \left(\frac{1}{4}\right)^i = \frac{1}{3}; \quad r_R = \sum_{i=1}^{\infty} \frac{1}{2} \left(\frac{1}{4}\right)^{i-1} = \frac{2}{3} \quad (2)$$

where  $i$  represents the iteration step. For the case shown in Fig. 2(a), the load distribution ratios are obviously equal to  $(1/2, 1/2)$ . The load distribution ratios for the broken bond in Fig. 2(c) can be derived using straightforward mathematical induction as

$$r_L = \frac{R}{L+R} \quad r_R = \frac{L}{L+R} \quad (3)$$

where  $L$  and  $R$  denote the distances to the left and right nearest surviving bonds from the broken bond.

### 2.2.2 One-Dimensional $n^{th}$ -Order GLLS Model

The  $n^{th}$ -order GLLS rule is used to describe general failure phenomena, where  $n$  corresponds to the size of the “damage zone”. The concept of the damage zone is employed to account for inelastic mechanisms, such as yielding, softening, and micro-cracking. The damage zone is centered around a broken bond  $i$  and for the  $n^{th}$ -order GLLS rule consists of  $n$  sites to the left and  $n$  sites to the right of bond  $i$ , denoted as  $\mathcal{D}_i = \{i-n, i-n+1, \dots, i-1, i+1, \dots, i+n\}$ . When bond  $i$  breaks, its nearest surviving bonds within the damage zone will share a certain ratio  $\xi$  ( $0 \leq \xi \leq 1$ ) of

the released load. This ratio  $\xi$  is calculated based on the algorithm described in the next subsection. The remaining ratio of the released load  $(1 - \xi)$  will be equally shared by all surviving bonds in the system. If there are no surviving bonds within the damage zone, the load will be equally shared by all surviving bonds in the system. When the size of the damage zone is equal to zero (i.e., no local interactions), the corresponding zeroth-order GLLS model reduces to the classical ELS model, where 100% of the load released by a broken bond is equally shared by all the surviving bonds in the system. At the other end of the spectrum, when the damage zone is as large as the entire system (i.e., extreme local interactions), the GLLS model becomes the ELLS model. As illustrated in the previous subsection, the ELLS rule corresponds to an extreme localization of load sharing, since all the load formerly carried by the broken bond is transferred only to the nearest surviving bonds. In this case, zero percent of the released load from a broken bond is equally shared by all surviving bonds in the system.

The localization parameter  $\xi$  is similar to parameter  $\lambda$  in the elastic beam model and indicates the degree of localization for a particular microstructure. For example, in a polymer composite,  $\xi$  depends on the shear lag behavior between the matrix and the reinforcement. Specifically,  $(1 - \xi)/\xi$  indicates the ratio between the global and local effects induced by a local failure.

### 2.2.3 Two-Dimensional $n^{th}$ -Order GLLS Model

The 2D GLLS model is developed around a 2D discrete lattice consisting of  $N_1 \times N_2$  bonds. Let  $\mathcal{S} = \{(i, j) | 1 \leq i \leq N_1, 1 \leq j \leq N_2\}$  index a discrete set of sites for the bonds on the rectangular lattice. Figure 3 shows two types of 2D nearest neighborhoods for a square array: (a) eight bonds in Moore's model [14] and (b) four bonds in Von Neumann's model [15]. In this work, the eight-bond Moore's model is selected for all cases considered. For each case in Fig. 3, the damage zone for the first-order GLLS rule is outlined by dashed lines, while for the second-order rule by bold lines. Note that the GLLS rule is not restricted to a square array. A hexagonal arrangement, for instance, can also be considered. For simplicity, all nearest-neighboring bonds in Moore's neighborhood are treated equally; i.e., one-eighth of the load from a broken bond is assigned to each nearest neighbor. Other non-uniform distribution schemes can be assigned, such as those based on Hedgepeth and Van Dyke's model [11].

To implement an  $n^{th}$ -order GLLS rule numerically in a 2D lattice system, a force-controlled quasi-static algorithm is described below. It is assumed that the strength of each bond is provided by randomly sampling from a given probability distribution with no correlation among the strengths of individual bonds. The elastic modulus of the bonds is assumed to be deterministic and identical for all bonds.

1. Determine the strength  $s_{kl}$ ;  $(k, l) \in \mathcal{S}$  of each bond by randomly sampling from a prescribed probability distribution. Initialize forces  $f_{kl}^{(0)} = f_0$  for every  $(k, l) \in \mathcal{S}$ . The value for  $f_0$  is selected so that no failures (breaks) are observed initially to any of the system's bonds.

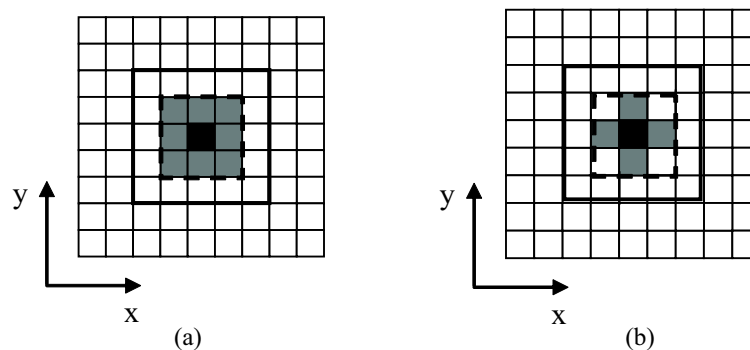


**FIG. 3:** Moore's neighborhood [gray area in (a)] and Von Neumann's neighborhood [gray area in (b)] of the broken bond (black square), with the first- and second-order damage zones indicated with dash and bold lines, respectively.

2. Identify the weakest bond  $(i, j)$  that is to be broken in the current loading step  $t$ :

$$(i, j) = \arg \max_{(k, l) \in S} \left( r_{kl} = \frac{f_{kl}^{(t)}}{s_{kl}} \right) \quad (4)$$

3. The total force on the entire system  $F^{(t)}$  is adjusted to a level leading to failure of the weakest bond  $(i, j)$  at the current loading step  $t$ :

$$F^{(t)} = \frac{1}{r_{ij}} \sum_{k=1}^{N_1} \sum_{l=1}^{N_2} f_{kl}^{(t)} \quad (5)$$

Compute the displacement  $u^{(t)} = F^{(t)} / (N_s \kappa)$ , where  $\kappa$  is the elastic modulus of the bonds and  $N_s$  is the number of surviving bonds. Update the force on the broken bond  $f_{ij}^{(t)} = 0$ .

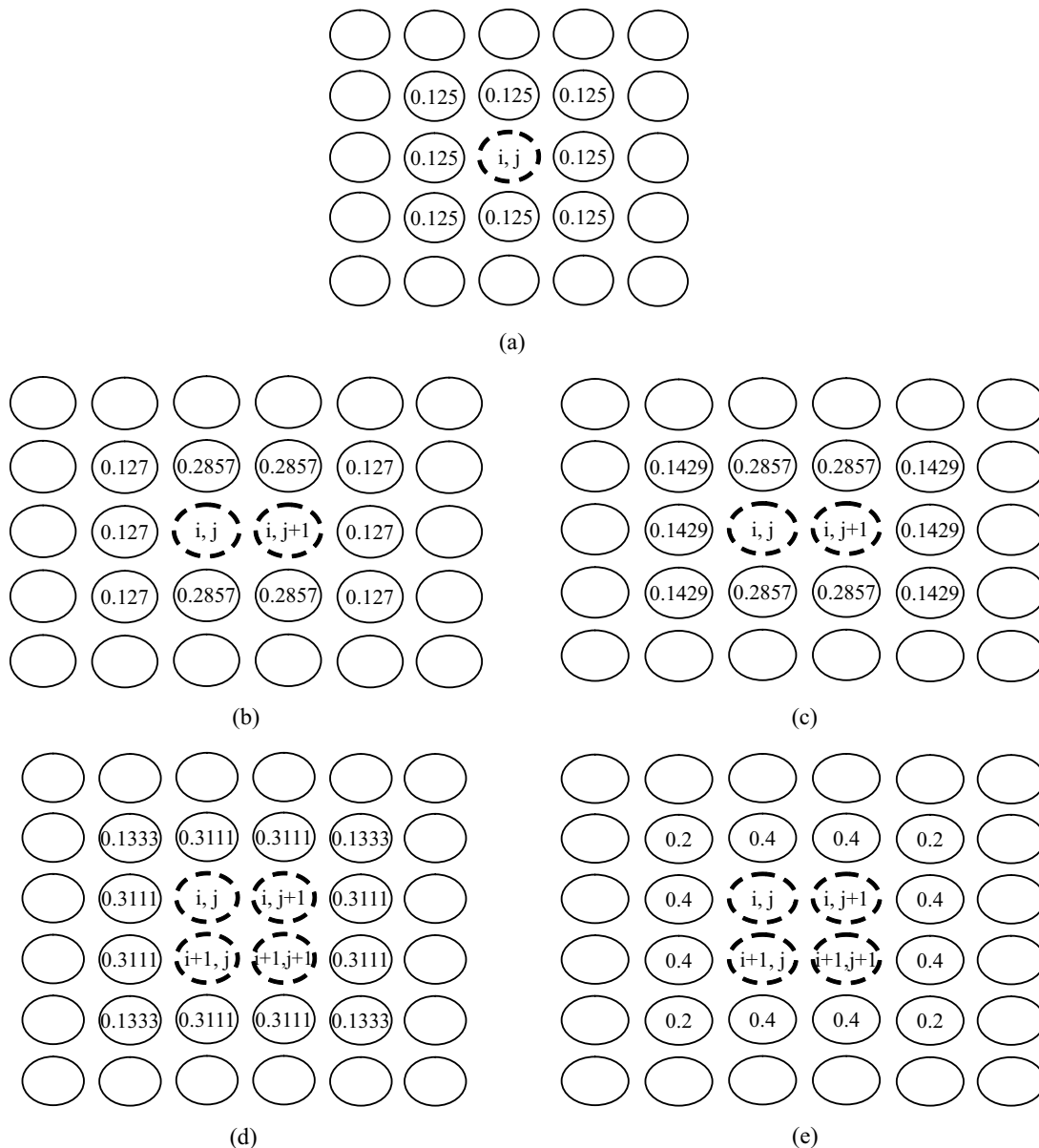
4. Identify the  $n^{th}$ -order damage zone  $\mathcal{D}_{ij}$  of the broken bond  $(i, j)$  (e.g., 24 bond sites for the second-order GLLS rule as shown in Fig. 3).
5. Distribute the load of the broken bond  $f_{ij}^{(t)}$  equally to all the bonds (intact or broken) in its nearest eight-bond Moore's neighborhood  $\mathcal{N}_{ij}$ . For any pre-existing broken bond  $(k, l) \in \mathcal{N}_{ij}$ , the load allocated to it is equally redistributed (i.e., one-eighth) to each bond of its own nearest eight-bond Moore's neighborhood  $\mathcal{N}_{kl}$  that belongs to  $\mathcal{D}_{ij}$ ; i.e.,  $\mathcal{N}_{kl} \cap \mathcal{D}_{ij}$ . This re-distribution process continues iteratively until the load shared by any pre-existing broken bond  $(p, q) \in \mathcal{D}_{ij}$  becomes negligibly small.
6. Sum up all the loads resulting from the redistribution described in the previous step to determine the percentage  $\xi$  of the load  $f_{ij}^{(t)}$  of the broken bond that has been redistributed within the damage zone  $\mathcal{D}_{ij}$ . Then distribute the remaining load  $(1 - \xi) \times f_{ij}^{(t)}$  equally to all the surviving bonds in the system.
7. Go back to Step 2 for the next loading step with all the updated forces.

#### 2.2.4 Illustrative examples involving the 2D $n^{th}$ -order GLLS model

- Example 1: Suppose that in the current load step bond  $(i, j)$  breaks and its nearest neighbors are all intact. Based on the first-order GLLS rule and the algorithm described in the previous section, the load distribution factors are calculated as shown in Fig. 4(a). Since there is no pre-existing broken bond in the nearest neighborhood,  $\xi = 1$  and all higher-order GLLS rules will yield the same results as the first-order rule.
- Example 2: Suppose two adjacent bonds  $(i, j)$  and  $(i, j+1)$  break simultaneously and all the bonds surrounding them are intact. The load distribution factors are shown in Figs. 4(b) and 4(c) based on the first- and second-order GLLS rules, respectively. It is also interesting to note the difference in the values of the localization parameter:  $\xi = 0.9524$  and  $\xi = 1$  for the first- and second-order rules, respectively. All higher-order GLLS rules will yield the same results as the second-order rule.
- Example 3: Suppose four adjacent bonds  $(i, j)$ ,  $(i, j+1)$ ,  $(i+1, j)$ ,  $(i+1, j+1)$  break simultaneously and all the bonds surrounding them are intact. The load distribution factors are shown in Figs. 4(d) and 4(e) for the first- and second-order GLLS rules, respectively. The  $\xi$  values for the two rules are 0.7555 and 1, respectively. All higher-order GLLS rules will yield the same results as the second-order rule.

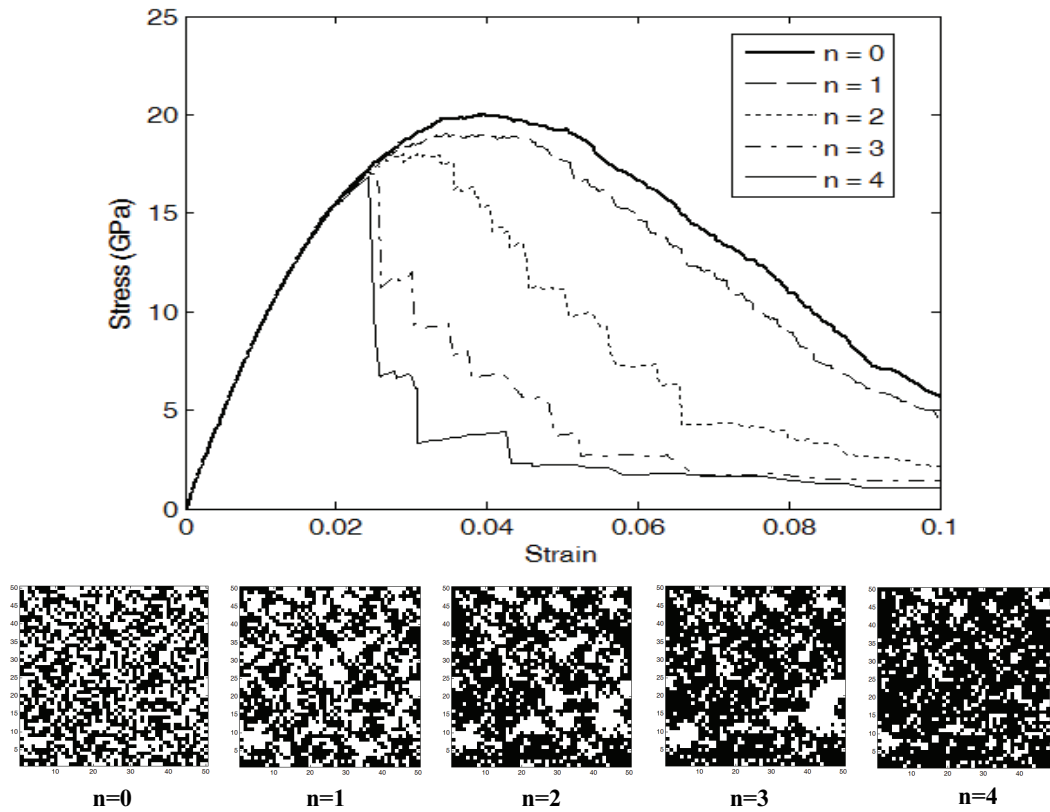
The above examples confirm the following behavior for the GLLS model that has been postulated: for a sufficiently high-order rule, that is when the damage zone is larger than the size of the cluster of breaks, load distribution and, hence, failure progression become "brittle-like" with localization parameter  $\xi = 1$ .

Figure 5 displays a sample set of five stress-strain curves and corresponding snapshots at the peak load for a  $50 \times 50$  lattice system using the force-controlled quasi-static iterative algorithm described earlier. The five curves and five



**FIG. 4:** Calculated load distribution factors (summing up to  $\xi$ , that can be less than unity) for examples involving: (a) a single broken bond; (b) two simultaneously broken bonds using the first-order rule; (c) two simultaneously broken bonds using the second-order rule; (d) four simultaneously broken bonds using the first-order rule; (e) four simultaneously broken bonds using the second-order rule.

snapshots provided correspond to five different orders of the GLLS rule. For direct comparison the five curves and snapshots correspond to the same sampling from a Weibull distribution for the strengths of the  $50 \times 50$  bonds of the lattice system. The Weibull distribution selected has a characteristic strength of 50 GPa and a shape parameter equal to 1.5 [refer to Eq. (8)]. The elastic modulus of the bonds is chosen to be equal to 1,000 GPa. The meaning of the coloring in the snapshots is the following: a black pixel indicates an intact bond while a white pixel indicates a broken bond. The snapshots indicate that as the GLLS order increases, the number of broken bonds at the peak load reduces.



**FIG. 5:** A sample set of five stress-strain curves and corresponding snapshots at the peak load for a  $50 \times 50$  lattice system. The five curves and snapshots correspond to five different orders of the GLLS rule. In the snapshots, a black pixel indicates an intact bond while a white pixel indicates a broken bond.

Figure 5 also indicates that as the GLLS order increases the localization effect becomes stronger, leading to a higher degree of brittleness.

### 3. MULTI-SCALE STOCHASTIC MODELING OF HIERARCHICAL STRUCTURE OF CNT FIBERS

#### 3.1 Hierarchical Structure of CNT Fibers

Due to the difficulty of dispersing CNTs homogeneously in a hosting matrix, micron-diameter CNT-based fibers have become an ideal candidate for harnessing the strength of CNTs in structural fiber-reinforced composites. These CNT fibers are fabricated by spinning millions of nanotubes; e.g.,  $10^5$ – $10^6$  multi-walled CNTs into a fiber with a diameter in the range of 5–20  $\mu\text{m}$  [16]. To improve the packing density and alignment, CNT fibers can be further post-processed with twisting, and a twisted fiber is also called a CNT yarn [17].

As illustrated in Fig. 6, a CNT fiber or yarn exhibits a hierarchical structure. At the lowest length scale are single-walled (or multi-walled) CNTs with nanoscale diameters (e.g., 1–10 nm) and micron-scale length (e.g., 10  $\mu\text{m}$ ). At the next length scale up are CNT bundles with diameters of e.g., 15–60 nm [18]. CNT bundles are naturally formed by approximately 10–100 aggregated CNTs [18, 19] due to van der Waals forces. Due to overlapping of individual tubes, the length of a CNT bundle is not well defined, and is generally up to a specific model to make an appropriate choice (e.g., 36–360  $\mu\text{m}$  following a shear lag model). At the final length scale are the CNT fibers with micron-scale diameters and a length similar to that of the bundles. A CNT fiber consists of thousands of CNT bundles that have formed a network or web with a preferred orientation along a CNT fiber axis. As a result of differences in fabrication



methods and fiber microstructure, the reported strengths of CNT fibers vary widely with values ranging from 3.3 GPa [20, 21] to 6.8 GPa [22]. These values are one order of magnitude lower than the strength of individual CNT's as reported, for example, by Yu et al. [23], Demczyk et al. [24], and Barber et al. [25].

Sensitivity to size and statistical variation in the strength of a CNT fiber demonstrated in experiments [22, 26] indicate that CNT fiber failure is a multi-scale stochastic phenomenon. The failure process of a micron-scale CNT fiber begins with the individual CNTs, which have been shown experimentally to have a strength following a Weibull distribution with a mean of the order of 100 GPa and a large coefficient of variation of the order of ~60% [25]. Growth of statistical atomic defects leads to failure of certain flawed CNTs (the ones with the lowest strengths from the Weibull distribution). The load released from a broken CNT is then transferred to neighboring CNTs within the CNT bundle via slippage due to low inter-tube shear strengths. When a relatively weak CNT bundle reaches its strength limit, its load will be distributed to neighboring CNT bundles. Consecutive failure of CNT bundles across the CNT fiber will eventually lead to failure of the entire CNT fiber.

Sensitivity to defects and flaws at multiple length scales is considered a major issue in the pursuit of robust design and fabrication of nanostructures. To further bridge the grand scale gap between CNTs and macroscopic composite structures, the major engineering challenge is building an efficient and robust multi-scale structure hierarchically based on models that account for uncertainty in material strength and structure. In addition to the uncertainty of atomic defects that will propagate up to the micron-scale fiber is the topological uncertainty at the bundle and fiber scales, such as bundle entanglement, chain ends, longitudinal variations of carbon contents (i.e., uncertainty in the number of CNTs and bundles), surface defects, etc. [21].

To demonstrate how uncertainty propagates across different length scales, the main objective of this work is to scale the effect of Weibull statistics of CNT strength [25] up to the micron-scale CNT fiber. A range of  $n^{th}$ -order GLLS rules is applied to simplify the complex topology associated with actual CNT fibers. Following the hierarchical structure of the CNT fibers illustrated in Fig. 6, the stochastic model used consists of two “up-scaling” processes [27]: CNT-to-CNT bundle and CNT bundle-to-CNT fiber, as detailed in the following two subsections.

### 3.2 Up-Scaling from CNT-to-CNT Bundle

#### 3.2.1 Statistical Strength of Individual CNTs of Length $l_t$

The characteristic length  $l_t$  and diameter  $d$  of individual single-walled CNT (SWCNTs) (refer to Fig. 6) are selected as

$$l_t = 10 \mu\text{m} \quad \text{and} \quad d = 1.7 \text{ nm} \quad (6)$$

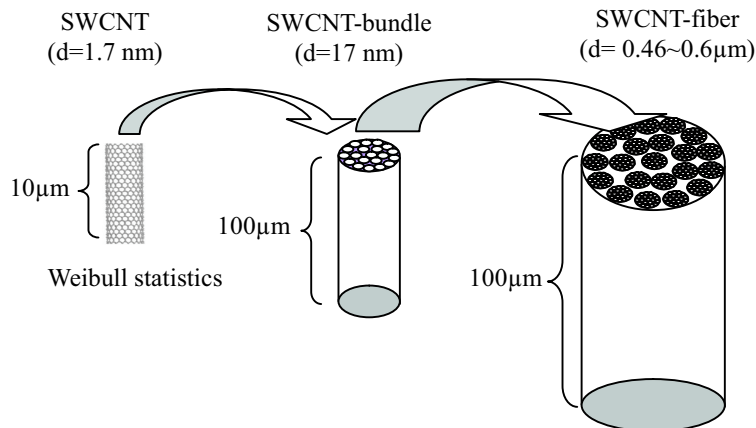


**FIG. 6:** Hierarchical structure of CNT fibers (the parameter values shown correspond to the actual values used in the simulation).

The strength  $S$  of an individual SWCNT with length  $l_t$  is modeled as a random variable assumed to follow a Weibull cumulative distribution function:

$$P_{\text{CNT}}(s) = 1 - \exp \left[ - \left( \frac{s}{s_t} \right)^\alpha \right] \quad (7)$$

where  $s_t$  is the characteristic strength and  $\alpha$  is the shape parameter. For the purposes of this study, the values of  $s_t$  and  $\alpha$  are selected as

$$s_t = 50 \text{ GPa} \quad \text{and} \quad \alpha = 1.5 \quad (8)$$

These numerical values for the characteristic strength and shape parameter correspond to a mean value of 45.1 GPa and a coefficient of variation (cov) of 67.9%.

### 3.2.2 Statistical Strength of CNT Bundles of Length $l_t$ (Up-Scaling from CNTs to CNT Bundles)

A CNT bundle is modeled here as  $10 \times 10 = 100$  individual CNTs assembled on a square grid and lying in parallel along a CNT bundle axis. At this stage, the length of the CNT bundle is considered to be equal to the length  $l_t = 10 \text{ }\mu\text{m}$  of an individual CNT. The strengths of these 100 individual CNTs are modeled as independent and identically distributed Weibull random variables with the parameters given in Eq. (8). The 2D  $n^{\text{th}}$ -order GLLS rule is used to model the failure of this CNT bundle. An individual CNT within the bundle behaves elastically until it breaks at its individual strength limit. The individual CNTs have a deterministic elastic modulus equal to 1,000 GPa that is assumed to be the same for all 100 CNTs.

Before using the 2D  $n^{\text{th}}$ -order GLLS rule on the  $10 \times 10 = 100$  bundle, the closed-form solution for the mean strength of a bundle consisting of an infinitely large number of individual CNTs following the ELS rule is considered for comparison purposes [7]:

$$\mu_{b-l_t}^\infty = s_t \left( \frac{1}{\alpha} \right)^{1/\alpha} \exp \left[ - \left( \frac{1}{\alpha} \right) \right] \quad (9)$$

Using the values for  $s_t$  and  $\alpha$  in Eq. (8), the mean strength of a bundle consisting of an infinite number of CNTs following the ELS rule is computed as

$$\mu_{b-l_t}^\infty = 19.6 \text{ GPa} \quad (10)$$

It should be noted that the corresponding standard deviation of the bundle strength asymptotically approaches zero as the number of individual CNTs approaches infinity.

To determine the corresponding mean bundle strengths according to the 2D zeroth-to-fourth-order GLLS rules on the  $10 \times 10 = 100$  CNT bundle, Monte Carlo simulations are performed using the force-controlled quasi-static iterative algorithm described earlier. The following results are obtained using 10,000 sample functions, a sufficient number to achieve convergence for all the orders considered

$$\mu_{b-l_t}^{(0)} = 20.8 \text{ GPa}; \text{ cov}^{(0)} = 9.1\% \quad (11a)$$

$$\mu_{b-l_t}^{(1)} = 20.2 \text{ GPa}; \text{ cov}^{(1)} = 9.2\% \quad (11b)$$

$$\mu_{b-l_t}^{(2)} = 19.7 \text{ GPa}; \text{ cov}^{(2)} = 9.6\% \quad (11c)$$

$$\mu_{b-l_t}^{(3)} = 19.5 \text{ GPa}; \text{ cov}^{(3)} = 9.9\% \quad (11d)$$

$$\mu_{b-l_t}^{(4)} = 19.5 \text{ GPa}; \text{ cov}^{(4)} = 10\% \quad (11e)$$

Although at this stage the length of the CNT bundle is equal to the length of an individual CNT ( $l_t = 10 \text{ }\mu\text{m}$ ), there is a significant drop both in the mean value and the coefficient of variation of the bundle strength when compared to the corresponding values for an individual CNT (having mean = 45.1 GPa and cov = 67.9%).

The mean bundle strength  $\mu_{b-l_t}^{(n)}$  decreases as the order of the GLLS rule increases, while the cov exhibits the opposite trend [Eq. (11)]. However, as indicated in Eq. (11), the effect of the order of the GLLS rule is relatively

minor. The mean bundle strength based on the zeroth-order GLLS (ELS) rule for the finite-size bundle considered here ( $\mu_{b-l_t}^{(0)} = 20.8$  GPa) is higher than the closed-form solution for the infinitely large system ( $\mu_{b-l_t}^{\infty} = 19.6$  GPa). Using a size effect justification, it can be claimed that the closed-form solution for the infinite-size system represents a lower bound for the strength of any zeroth-order GLLS (ELS) finite-size system.

Using the generated strength values from the aforementioned Monte Carlo simulations (10,000 values for each order of the GLLS rule), it is possible to estimate which probability distribution these values follow. The normal probability paper plot in Fig. 7 indicates that the bundle strengths are not Gaussian (after all, strength is a physical quantity that only takes non-negative values). This estimated non-Gaussian probability distribution of the strength of a CNT bundle of length  $l_t$  is denoted by  $P_{b-l_t}(s)$ .

At this juncture, it should be mentioned that although the CNT bundles considered in this study consist of  $10 \times 10 = 100$  individual CNTs arranged on a square grid, it is customary to consider that CNT bundles are circular. For this purpose, an "equivalent" circular CNT bundle can be defined with a diameter of 17 nm as indicated in Fig. 6. The main conclusion of this part of the up-scaling process (going from individual CNTs of length  $l_t = 10 \mu\text{m}$  to  $10 \times 10$  CNT bundles of the same length  $l_t$ ) is that there is a significant drop both in the mean value and the coefficient of variation of the bundle strength when compared to the corresponding values for an individual CNT.

### 3.3 Up-Scaling from CNT Bundle to CNT Fiber

#### 3.3.1 Statistical Strength of CNT Bundles of Length $l_b$

The length  $l_b$  of the CNT fibers is one order of magnitude larger than the characteristic length  $l_t$  of individual CNTs. As  $l_t$  was assumed to be  $10 \mu\text{m}$  in Eq. (6), the length of the CNT fibers is set equal to

$$l_b = 100 \mu\text{m} \quad (12)$$

The first step in up-scaling from the CNT bundle of length  $l_t$  (examined in the previous section) to the CNT fiber of length  $l_b$  is to up-scale from a CNT bundle of length  $l_t$  to a CNT bundle of length  $l_b$ . This is accomplished using the smallest value exact distribution of extremes (weakest link model).

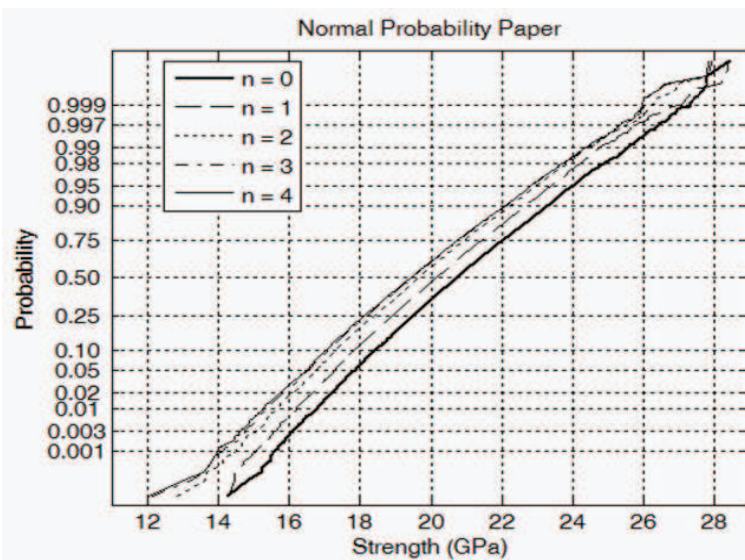


**FIG. 7:** Normal probability paper plot for the strengths of CNT bundles of length  $l_t = 10 \mu\text{m}$  obtained using the 2D zeroth-to-fourth-order GLLS rules on  $10 \times 10$  CNT bundles (10,000 values are plotted for each order of the GLLS rule).

Denoting the probability distribution of the strength of a CNT bundle of length  $l_b$  by  $P_{b-l_b}(s)$ , its functional form is given by

$$P_{b-l_b}(s) = 1 - [1 - P_{b-l_t}(s)]^{l_b/l_t} \quad (13)$$

Using Eq. (13) and the five probability distributions for  $P_{b-l_t}(s)$  established in Fig. 7 for the five different orders of the GLLS rule, the resulting probability distributions  $P_{b-l_b}(s)$  for the strength of a CNT bundle of length  $l_b$  are plotted in Fig. 8. The corresponding mean values and coefficients of variation are given by

$$\mu_{b-l_b}^{(0)} = 17.9 \text{ GPa}; \quad \text{cov}^{(0)} = 6.2\% \quad (14a)$$

$$\mu_{b-l_b}^{(1)} = 17.3 \text{ GPa}; \quad \text{cov}^{(1)} = 6.4\% \quad (14b)$$

$$\mu_{b-l_b}^{(2)} = 16.7 \text{ GPa}; \quad \text{cov}^{(2)} = 6.8\% \quad (14c)$$

$$\mu_{b-l_b}^{(3)} = 16.6 \text{ GPa}; \quad \text{cov}^{(3)} = 7.1\% \quad (14d)$$

$$\mu_{b-l_b}^{(4)} = 16.5 \text{ GPa}; \quad \text{cov}^{(4)} = 7.1\% \quad (14e)$$

As the smallest value exact distribution of extremes was used (weakest link model), there is a drop both in the mean value and the coefficient of variation of the strength of the bundle of length  $l_b$  [Eq. (14)], when compared to the corresponding values for the strength of the bundle of length  $l_t$  [Eq. (11)].

### 3.3.2 Statistical Strength of CNT Fibers of Length $l_b$ (Up-Scaling from CNT Bundles to CNT Fibers)

A CNT fiber of length  $l_b = 100 \mu\text{m}$  is modeled here in the following way: a  $50 \times 50 = 2,500$  square grid is considered, but unlike the case of the  $10 \times 10 = 100$  square grid considered for the CNT bundle, not all 2,500 locations are filled with CNT bundles now. This is done to account for the well-known low packing density  $\rho_b$  of CNT fibers. Two cases are considered: one with a packing density of  $\rho_b = 50\%$  (1,250 CNT bundles randomly distributed over the 2,500 grid locations) and one with a packing density of  $\rho_b = 30\%$  (750 CNT bundles randomly distributed over

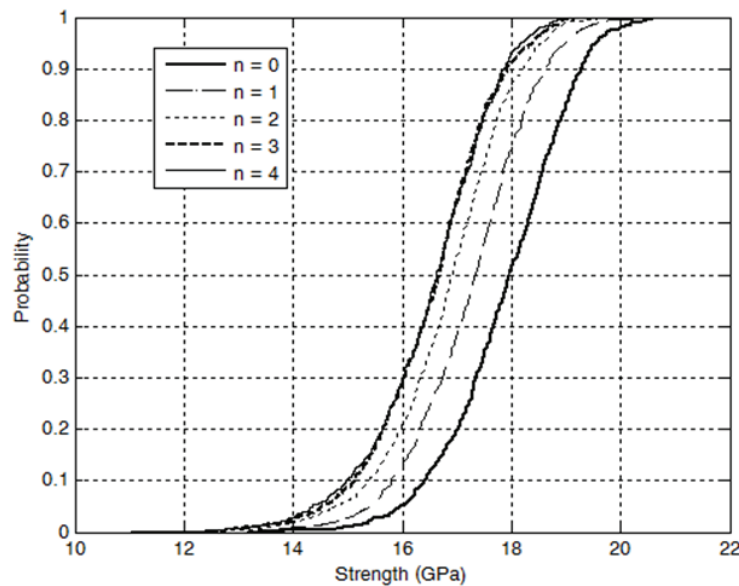


**FIG. 8:** Probability distributions for the strengths of CNT bundles of length  $l_b = 100 \mu\text{m}$  obtained using the 2D zeroth-to-fourth-order GLLS rules on  $10 \times 10$  CNT bundles.

the 2,500 grid locations). The strengths of the individual CNT bundles are modeled as independent and identically distributed random variables following the distributions shown in Fig. 8 (depending on the order of the GLLS rule used to establish the strength of the CNT bundles).

To determine the probability distribution of the strength of the CNT fibers according to the 2D zeroth-to-third-order GLLS rules on the  $50 \times 50 = 2,500$  CNT fiber, Monte Carlo simulations are performed again using the force-controlled quasi-static iterative algorithm described earlier (using 5,000 samples for each case). It is obvious that for every combination of a packing density value and an order of the GLLS rule used on the  $50 \times 50 = 2,500$  CNT fiber grid four different probability distributions can be computed for the strength of the CNT fibers, each one corresponding to a different GLLS rule used on the underlying  $10 \times 10 = 100$  CNT bundle grid. For simplicity, only two of these four probability distributions are kept: one is called the upper estimate and the other the lower estimate (the intermediate ones are not considered in this study).

At this juncture, it should be mentioned that although the CNT fibers considered in this study are based on a  $50 \times 50$  square grid, it is customary to consider that CNT fibers are circular. For this purpose, an "equivalent" circular CNT fiber can be defined with a diameter of  $0.60 \mu\text{m}$  for the case of packing density  $\rho_b = 50\%$  and  $0.46 \mu\text{m}$  for  $\rho_b = 30\%$ , as indicated in Fig. 6.

Figures 9 and 10 depict the resulting probability distributions for the strengths of the CNT fibers with  $\rho_b = 50\%$  and  $30\%$ , respectively (based on 5,000 simulated values for each case), while Table 1 provides the corresponding mean values and coefficients of variation. The normal probability paper plots in Figs. 9 and 10 indicate that the CNT fiber strengths are not following a Gaussian distribution (only the zeroth-order GLLS rule yields curves that are reasonably close to the Gaussian except for their left tails). Table 1 indicates a decrease in the mean value of the strength as the order of the GLLS rule increases, and the opposite trend is observed for the coefficient of variation.

The main conclusion of this part of the up-scaling process (going from individual CNT bundles of length  $l_b$  to CNT fibers of the same length) is that there is a significant drop in the mean values of the fiber strength (Table 1) compared to the corresponding values of the bundle strength [Eq. (14)].

It is very difficult to make direct comparisons of our numerically established results for fiber strength (Table 1) with tensile test data, as it is practically impossible to ensure that the exact same types of CNT fibers are compared. Consequently, the experimental results provided in the following should be used with great caution and certainly not

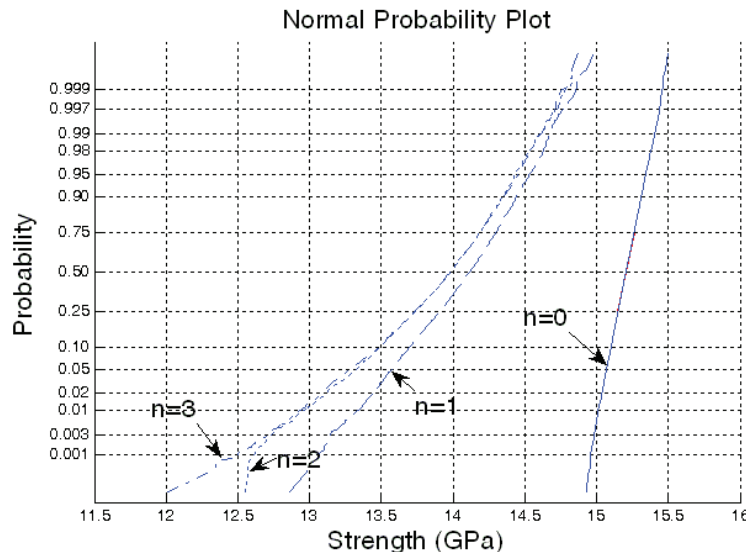


**FIG. 9:** Normal probability paper plots for the upper strengths of CNT fibers of length  $l_b = 100 \mu\text{m}$  obtained using the 2D zeroth-to-third-order GLLS rules on  $50 \times 50$  CNT fibers. Plot obtained using  $\rho_b = 50\%$  and the 2D zeroth-order GLLS rule on the  $10 \times 10$  CNT bundles. Each curve involves 5,000 simulated points. Case identified in Table 1 as  $\rho_b = 50\%$  (upper estimate).

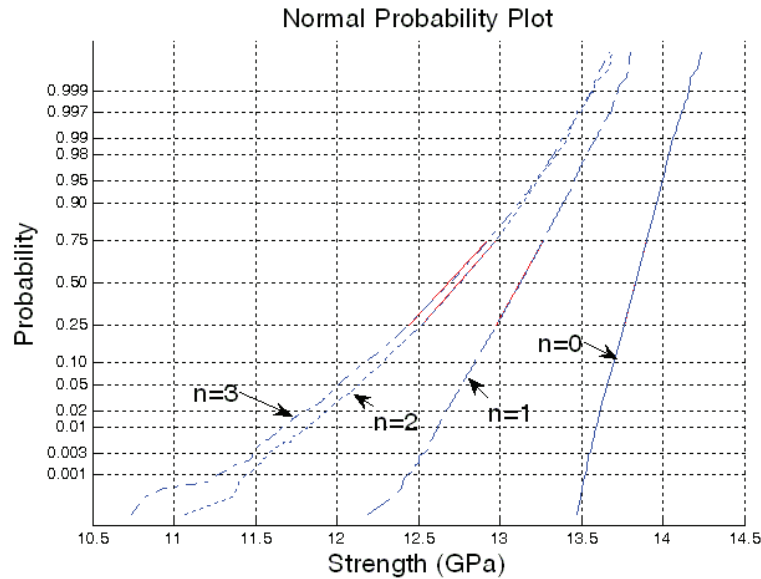


**FIG. 10:** Normal probability paper plots for the lower strengths of CNT fibers of length  $l_b = 100 \mu\text{m}$  obtained using the 2D zeroth-to-third-order GLLS rules on  $50 \times 50$  CNT fibers. Plot obtained using  $\rho_b = 30\%$  and the 2D fourth-order GLLS rule on the  $10 \times 10$  CNT bundles. Each curve involves 5,000 simulated points. Case identified in Table 1 as  $\rho_b = 30\%$  (lower estimate).

**TABLE 1:** Mean values and coefficients of variation for the strength of CNT fibers of length  $l_b = 100 \mu\text{m}$  estimated from 5,000 simulated samples in each case.

		GLLS rule used on the $50 \times 50$ CNT fibers			
	GLLS rule used on the $10 \times 10$ CNT bundles	$\mu_f^{(0)}$ (GPa)/cov	$\mu_f^{(1)}$ (GPa)/cov	$\mu_f^{(2)}$ (GPa)/cov	$\mu_f^{(3)}$ (GPa)/cov
$\rho_b = 50\%$ (upper estimates)	zeroth-order	15.2/0.54%	14.1/2.1%	13.9/2.5%	13.9/2.5%
$\rho_b = 50\%$ (lower estimates)	fourth-order	13.8/0.58%	12.7/2.2 %	12.6/2.6%	12.6/2.7%
$\rho_b = 30\%$ (upper estimates)	zeroth-order	15.2/0.70%	14.5/1.6 %	14.1/2.6%	14.0/2.7%
$\rho_b = 30\%$ (lower estimates)	fourth-order	13.8/0.76%	13.1/1.6 %	12.7/2.7%	12.7/2.9%

for a direct comparison with our numerical results. A first set of test data by Li et al. [22] considered CNT fibers with diameters in the range of  $7.6\text{--}21.1 \mu\text{m}$  (in contrast, our fibers have diameters of  $0.46\text{--}0.60 \mu\text{m}$ ), packing density of bundles around 48% (one of our cases considers 50%, which is quite close to 48%), and a length of 10 mm (our fibers have a length of only  $100 \mu\text{m} = 0.1 \text{ mm}$ ). Li et al. [22] tested six CNT fiber samples of this type and reported strengths from 1.1 to 6.8 GPa. A second set of test data by Ma et al. [26] considered CNT fibers with a packing density of bundles in the range of 30%–50%, but there was no mention about the diameter or length of these fibers. In this work, the reported strengths were in the range of 0.9–1.6 GPa for epoxy infiltrated fibers and 0.7–1.3 GPa for poly-vinyl-alcohol infiltrated fibers. It is interesting to note the significant differences between these two sets of experimental data (most probably due to the fact that the CNT fibers tested were quite different). The important conclusion here is that our

numerically established values for the CNT fiber strengths are in the same general range as the experimental results. Any more direct comparison beyond this statement of “in the same general range” would be meaningless considering that: (1) there are very significant differences in the diameters and lengths of the fibers used in the experiments versus those used in this paper; (2) all the strengths in this paper are determined using true (solid) cross-sectional areas, while in the experimental works nominal cross-sections are used that incorporate the void parts of the cross-section as a solid part; and (3) there might be other critical differences not clearly specified in the literature in the overall configuration of the fibers used in the experiments versus the corresponding configuration of the fibers considered in this paper. The following general conclusions can be drawn now considering the entire up-scaling process from the individual CNT to the CNT bundle and then to the CNT fiber: (1) there is a very significant reduction in strength from a value of 45.1 GPa for an individual CNT to approximately 12.6–15.2 GPa (Table 1) for a CNT fiber, and (2) there is an equally significant reduction in the coefficient of variation of the strength from a value of 67.9% for the individual CNT to approximately 0.54–2.9% (Table 1) for a CNT fiber. It should be noted here that this numerically established cov range of 0.54–2.9% for the strength of the CNT fibers is considered relatively low, as experimental results usually indicate higher values [22]. It is believed that this is due to a series of simplifying assumptions made in this work, including bundle packing density constant along the length, fiber packing density constant from fiber to fiber, assumption of independence for the random variables modeling the strengths of individual CNTs and individual CNT bundles, etc. It is expected that when these assumptions are relaxed in a future study, the coefficient of variation of the fiber strength will increase.

#### 4. CONCLUSIONS AND FUTURE WORK

In this study a GLLS model is introduced to study the statistical strength of a micron-scale CNT fiber, a nanocomposite consisting of a hierarchical structure of CNTs aligned into CNT bundles, and CNT bundles aligned into a CNT fiber. The basic result of the model indicates that the mean strength reduces by approximately two-thirds of an order of magnitude when up-scaling from a nanoscale CNT (1.7 nm in diameter and 10  $\mu\text{m}$  in length) to a micron-scale CNT fiber (0.46~0.60  $\mu\text{m}$  in diameter and 100  $\mu\text{m}$  in length). This strength reduction occurs at three different stages of the up-scaling process: (1) up-scaling from individual CNTs of length  $l_t$  to CNT bundles of the same length; (2) up-scaling from a CNT bundle of length  $l_t$  to a CNT bundle of length  $l_b$  ( $l_b = 10l_t$ ); and (3) up-scaling from CNT bundles of length  $l_b$  to CNT fibers of the same length. The specific strength reductions during these three stages are provided in the paper.

The multi-scale stochastic model developed in this work accounts for a number of sources of uncertainty common to most nanocomposites [21]:

1. Uncertainty due to atomic defect distribution, represented by Weibull statistics for the strength of individual CNTs.
2. Bundle entanglement and misalignment, accounted for by varying the order of the GLLS rule.
3. Effect of spatially random distribution of CNTs within the CNT bundle, considered by using a Monte Carlo approach to randomly distribute CNTs of randomly varying strength within the bundle grid.
4. Statistical size effect of CNT bundle strength accounted for through a weakest link model (exact distribution of extremes).
5. Effect of spatially random distribution of CNT bundles and voids within the CNT fiber, considered by using a Monte Carlo approach to randomly distribute CNT bundles of randomly varying strength within the fiber grid.

Future work will include the investigation of the following issues for a more thorough quantification of the CNT fiber strength uncertainty (especially of its coefficient of variation that is currently predicted to be lower than what experiments indicate):

1. Effect of random variation of carbon content along the fiber axis.

2. Effect of random variation of fiber diameter and of bundle size.
3. Three-dimensional GLLS modeling using load transfer factors along the bundle and fiber axes.
4. Use of a random field model [28] to better model the random distribution of CNTs within a CNT bundle of arbitrary length and of CNT bundles within a CNT fiber.
5. Effect of bundle clustering when up-scaling from a CNT bundle to a CNT fiber.

## ACKNOWLEDGMENTS

X. F. Xu and K. Hu acknowledge the support provided by the Department of Energy under Award No. DE-FG02-06ER25732 of the Early Career Principal Investigator Program. I. J. Beyerlein acknowledges support provided by the Los Alamos National Laboratory Directed Research and Development (LDRD) project DR20110029. G. Deodatis acknowledges the support provided by the National Science Foundation under Grant No. CMMI-0928129 with Dr. Mahendra P. Singh as Program Director.

## REFERENCES

1. Zabaras, N., and Ganapathysubramanian, B., A scalable framework for the solution of stochastic inverse problems using a sparse grid collocation approach, *J. Comput. Phys.*, 227:4697–4635, 2008.
2. Liu, W. K., Qian, D., Gonella, S., Li, S. F., Chen, W., and Chirptukar, S., Multiscale methods for mechanical science of complex materials: Bridging from quantum to stochastic multiresolution continuum, *Int. J. Numer. Methods Eng.*, 83(8–9):1039–1080, 2010.
3. Fish, J. and Wu, W., A nonintrusive stochastic multiscale solver, *Int. J. Numer. Methods Eng.*, 88(9):862–879, 2011.
4. Arnst, M. and Ghanem, R., Probabilistic equivalence and stochastic model reduction in multiscale analysis, *Comput. Methods Appl. Mech. Eng.*, 197(43–44):3584–3592, 2008.
5. Xu, X. F., A multiscale stochastic finite element method on elliptic problems involving uncertainties, *Comput. Methods Appl. Mech. Eng.*, 196:2723–2736, 2007.
6. Xu, X. F., Chen, X., and Shen, L., A green-function-based multiscale method for uncertainty quantification of finite body random heterogeneous materials, *Comput. Struct.*, 87:1416–1426, 2009.
7. Daniels, H. E., The statistical theory of the strength of bundles of threads, *Proc. Royal Soc. London, Series A, Math. Phys. Sci.*, 183:405–35, 1945.
8. Harlow, D. G. and Phoenix, S. L., Probability distributions for the strength of composite materials I: Two-level bounds, *Int. J. Fract.*, 17:347–372, 1981.
9. Harlow, D. G. and Phoenix, S. L., Probability distributions for the strength of composite materials II: A convergent sequence of tight bounds, *Int. J. Fract.*, 17:601–30, 1981.
10. Phoenix, S. L. and Beyerlein, I. J., Distributions and size scalings for strength in a 1D random lattice with load redistribution to nearest and next-nearest neighbors, *Phys. Rev.*, 62:1622–1645, 2000.
11. Hedgepeth, J. M. and Van Dyke, P., Local stress concentration in imperfect filamentary composite materials, *J. Compos. Mater.*, 1:294–309, 1967.
12. Beyerlein, I. J. and Phoenix, S. L., Stress concentrations around multiple fiber breaks in an elastic matrix with local yielding or debonding using quadratic influence superposition, *J. Mech. Phys. Solids*, 44:1997–2039, 1996.
13. Belytschko, T. and Mish, K., Computability in non-linear solid mechanics, *Int. J. Numer. Methods Eng.*, 52:3–21, 2001.
14. Wolfram, S., Statistical mechanics of cellular automata, *Rev. Mod. Phys.*, 55:601–44, 1983.
15. Van Neumann, J., *Theory of Self-Reproducing Automata*, A. Burks, ed., Univ. of Illinois Press, Urbana, IL, 1966.
16. Zhang M., Atkinson, K. R., and Baughman, R. H., Multifunctional carbon nanotube yarns by downsizing an ancient technology, *Science*, 306:1358–1361, 2004.
17. Beyerlein, I. J., Porwal, P. K., Zhu, Y. T., Hu, K., and Xu, X. F., Scale and twist effects on the strength of nanostructured yarns and reinforced composites, *Nanotechnol.*, 20:485702, 2009.



18. Behabtu, N., Green, M. J., and Pasquali, M., Carbon nanotube-based neat fibers, *Nanotoday*, 3:24–34, 2008.
19. Tran, C. D., Humphries, W., Smith, S. M., Huynh, S. M., and Lucas, S., Improving the tensile strength of carbon nanotube spun yarns using a modified spinning process, *Carbon*, 47:2662–2670, 2009.
20. Zhang, X., Li, Q., Holesinger, T. G., Arendt, P. N., Huang, J., Kirven, P. D., Clapp, T. G., DePaula, R. F., Liao, X., Zhao, Y., Zheng, L., Peterson, D. E., and Zhu Y., Ultrastrong, stiff, and lightweight carbon-nanotube fibers, *Adv. Mater.*, 19:4198–4201, 2007.
21. Koziol, K., Juan, V., Anna, M., Marcelo, M., Philip, C., Michael, S., and Alan, W., High-performance carbon nanotube fiber, *Science*, 318:1892–1895, 2007.
22. Li, F., Cheng, H. M., Bai, S., Su, G., and Dresselhaus, M. S., Tensile strength of single-walled carbon nanotubes directly measured from their macroscopic ropes, *Appl. Phys. Lett.*, 77:3161–3163, 2000.
23. Yu, M.-F., Bradley, S. F., Sivaram, A., and Rodney, S. R., Tensile loading of ropes of single wall carbon nanotubes and their mechanical properties, *Phys. Rev. Lett.*, 84:5552–5555, 2000.
24. Demczyk, B. G., Wang, Y. M., Cumings, J., Hetman, M., Han W., Zettl, A., and Ritchie, R. O., Direct mechanical measurement of the tensile strength and elastic modulus of multiwalled carbon nanotubes, *Mater. Sci. Eng.*, 334:173–178, 2002.
25. Barber, A. H., Kaplan-Ashiri, I., Cohen, S. R., Tenne, R., and Wagner, H. D., Stochastic strength of nanotubes: An appraisal of available data, *Compos. Sci. Technol.*, 65:2380–2384, 2005.
26. Ma, W., Liu, L., Zhang Z., Yang, R., Liu, G., Zhang, T., An, X., Yi, X., Ren, Y., Niu, Z., Li, J., Dong, H., Zhou, W., Pulickel, M. A., and Xie, S., High-strength composite fibers: Realizing true potential of carbon nanotubes in polymer matrix through continuous reticulate architecture and molecular level couplings, *Nano Lett.*, 9(8):2855–2861, 2009.
27. Hu, K. and Xu, X. F., Probabilistic upscaling of material failure using random field models—A preliminary investigation, *Algorithms*, 2:750–763, 2009.
28. Shi, Y., Deodatis, G., and Betti, R., Random field-based approach for strength evaluation of suspension bridge cables, *ASCE J. Struct. Eng.*, 133:1690–1699, 2007.
29. Yokobson, B. I., Samsonidze, G., and Samsonidze, G. G., Atomistic theory of mechanical relaxation in fullerene nanotubes, *Carbon*, vol. 38:1675–1680, 2000.